JOURNAL OF MATERIALS SCIENCE **33** (1998) 3907–3918

Solidification behaviour of Al–7% Si–0.3% Mg during rotary spray forming

A. E. W. JARFORS
Royal Institute of Technology, Department of Materials Processing,
100 44 Stockholm, Sweden
E-mail: andersj@matpr.kth.se

The solidification behaviour of an Al–7% Si–0.3% Mg alloy during rotary spray forming was studied. The ability to form a coating was insensitive to the thermal processing parameters, yielding material exchangess greater than 90%. The level of porosity varied typically between 1.5 and 4.75%. The dendrite arm spacing was evaluated and used to estimate the cooling rates. Typical dendrite secondary arm spacings were of the order of 3 μm, 12 μm and 25 μm, corresponding to cooling rates of 4630 $\mathrm{K\,s^{-1}}$, 72 $\mathrm{K\,s^{-1}}$ and 8 $\mathrm{K\,s^{-1}}$, respectively. The fraction primary precipitation was experimentally determined and the partition coefficient calculated indirectly using the Scheil equation. The partition coefficient is increased during rotary spray forming. This is explained by the presence of trapped vacancies at the solidification front. The vacancies change the solid's free energy and thus change the phase diagram and the partition coefficient. A simplistic analysis of entrapment and condensation of vacancies and their influence on the partition coefficient is made. © *1998 Kluwer Academic Publishers*

1. Introduction

Spray forming is an attractive method having the typical attributes of producing fine microstructures and macrosegregation-free materials. Spray forming has mostly been made using gas-assisted methods such as Osprey$^{\mathrm{TM}}$ [1, 2] and liquid dynamic compaction [3–6]. These methods have been successfully used to make both traditional materials and metal matrix composites [2, 6, 7]. Spray-formed material is now commercially available. The typical nature of the gas-assisted methods is high particle velocities, rapid cooling during flight and moderate cooling rates on impact on the substrate [3–5]. These gas-assisted methods have, however, some limitations. One limitation is the massive use of high-purity gases such as nitrogen and argon, which are costly. A second limitation is the dissolution and entrapment of gas into the sprayed layer, causing porosity. This is not always a problem since nitrogen may be used as an alloying element in steel. A third limitation is the fact that not all types of material can be produced, without extreme difficulty, in gas-assisted methods because of reactivity. A better method such as a rotary spraying technique would here be advantageous [8, 9]. Again rotary spray forming also enables the use of reactive atmospheres to make *in-situ* composites since an atmosphere of controlled partial pressure can be used during spraying. The difficulty of rotary spray forming is the control of the spray direction. It has, however, been shown that it is possible to reduce the spread in the hoop direction when using a rotating disc as atomizer, and thus a focused spray may be obtained [9].

2. Rotary spray forming

The present work is based on the use of a rotary spray former being developed [9] with the main purpose of making low-fraction *in-situ* composite materials or dispersion-strengthened material. Rotary spraying and atomization have been used for a long time [10, 11] in the field of powder manufacturing. The main advantage is the narrow distribution of powder particles and thus homogeneous thermal history and compressive properties. Compared with gas-assisted methods it is unlikely that gas-assisted methods will be successful in the manufacturing of *in-situ* composite materials, with fair amounts of reinforcement, owing to the rapid cooling during flight. The rapid cooling provides too short a time for a substantial reaction to take place in a controlled manner. To obtain a substrate free from porosity the process is sensitive to gas entrapment and the degree of solidification of the spray on impact. This is due to the formation of surface irregularities and flow of metal, as well as gas on impact. In rotary spraying, the relative velocity between the droplets and gas is lower and thus the cooling rate is less. It is furthermore possible to spray under vacuum or in a highly reactive atmosphere.

The present work deals with the solidification characteristics of the process using an aluminium alloy as a model material. The cooling rates are estimated, and the microstructure is studied. The sensitivity of the process to the processing parameters is investigated to access the feasibility of having a large amount of melt on the substrate to facilitate a reaction after droplet impact. This is because a reaction after impact may be used to increase the fraction of the reinforcement. The solidification of the aluminium alloy itself is also investigated owing to the special properties of the process and thus the possibility of manufacturing traditional material with new properties. This is mainly due to the possibility of supersaturation of the matrix and microstructural refinement obtained during spraying.

The present spray former has been described elsewhere [9] and will not be treated in depth in the present work. It should, however, be mentioned that the spray characteristic of the apparatus is that three different modes for the droplet formation exist. At the rim of the disc, in the main stream of metal, a film is formed that is disintegrated. This is the origin of a moderately sized droplet stream. After this disintegration, the remaining liquid on the disc surface, transported to the edge of the disc, is not sufficient to maintain the existence of the film. This alters the disintegration mechanism to a direct drop formation at the disc edge. This mechanism produces a much finer droplet size distribution. The third mechanism is a disturbance where droplets are flung from the point of impact slightly directed upwards. This mode is undesired and may be controlled using the appropriate rates of rotation and mass discharges. In general the fine droplets are present at all mass discharges, while the coarse drops are only present at high mass discharges.

3. Experimental procedure

The aim of the series of experiments was to test the feasibility of using a centrifugal spray former as a means for coating with a directed spray. The chemical composition of the aluminium alloy is specified in Table I.

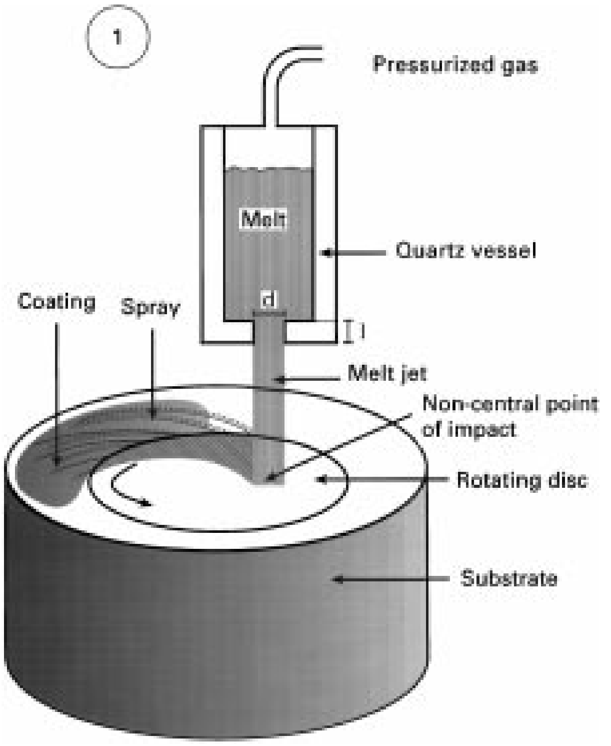

Figure 1 Schematic diagram of the rotary spray former.

The experimental set-up is schematically shown in Fig. 1. The experiments were made with a cylindrical substrate surrounding the atomizer unit. The experimental conditions can be found in Table II. The procedure for the aluminium spraying experiments are inclusive of shot peening the copper substrate and measuring the surface roughness to ascertain a constant surface roughness between each experiment. Before each experiment the alloy, crucible, thermocouple and substrate were weighed to have a reference point for the efficiency of sticking to the substrate. The sticking efficiency was then defined as the ratio of the weight increase of the substrate to the original weight of the alloy minus the unsprayed mass (material remaining in the quartz tube and on the thermocouple). The experimental set-up was mounted and the alloy was heated to the experimental temperature. As this temperature was reached, pressurized gas was let into the crucible and a melt jet was sprayed onto the atomizer and sprayed on the substrate. The spray consisted usually of fine droplets and medium-sized droplets, but sometimes a minor fraction of coarser droplets had formed. The majority of the spray consisted of the medium-sized droplets and a minority of the fine-sized droplets. The region for deposition of the medium-sized droplets was normally relatively well focused and defined the circumferential spread. The finer droplets tended to be more spread in the hoop direction. The metallographic investigation of the coating was made to measure the level of porosity. The metallographic investigation furthermore yielded the fraction of primary phase and secondary dendrite arm spacing as a function of the distance from the deposition substrate. The metallographic investigation was made in a cross-section of the deposited layer at the centre of the focused main spray region. All measurements are thus made on the deposit and not on the sprayed droplets. The changes found in the deposit are thus secondary effects from the atomization originating from droplet in-flight solidification and spray mass discharge. The porosity level was measured using a 20 × 20 grid and counting the

TABLE I Material data

Material		Composition (%)										
		Al	Cu	Fe	Mg	Mn	Ni	Pb	Si	Sn	Ti	Zn
Aluminium alloy	Nominal	Balance	—	—	0.3	—	—	—	7	—	—	—
(SS4244)	Maximum	Balance	—	—	0.4		—	—	7.5	—	—	—
(Al–7% Si–0.3% Mg)	Minimum	Balance	0.2	0.5	0.2	0.5	0.1	0.05	6.5	0.05	0.2	0.3

TABLE II Experimental conditions, where the point of impact on the disc was located at a radius of 0.8 cm from the centre, the disk radius was in all experiments 1.16 cm, and the jet length before impact was 1 cm in all experiments

Experiment	T-spray (°C)	ΔP (atm)	Rate of rotation (per min^{-1})	d 10^2 m	$1/d$	Remarks
SG1A1S1	> 808	0.4	30 000	0.7	4.28	[a, b]
SG1A1S2	1183	0.9	30 000	0.7	5.71	[a]
SG4A1S3	≈ 900	0.1	30 000	0.7	1.43	[b]
SG5A1S4	≈ 900	0.5	30 000	0.7	5.71	[b, c]
SG3A1S5	950	1.0	30 000	0.7	5.71	
SG6A1S7	660	< 0.1	30 000	0.7	5.71	
SG7A1S8	860	0.1	15 000	0.1	8.57	
SG8A1S9	850	0.1	40 000	0.7	4.28	[d]
SG9A1S11	950	0.1–0.2	15 000	0.7	5.00	[e]
SG1A1S13	860	0.1	30 000	0.7	5.71	
SG10A1S12	952	0.1	40 000	0.7	5.71	
SG6A1S14	≈ 950	0.1	20 000	0.7	8.57	[b]
SG6A6S15	1048	0.1	30 000	0.7	3.57	

[a] Pressure was continuously increased to obtain a spray.
[b] Thermocouple broken.
[c] Possible temperature drop at the end of the spray sequence.
[d] Nozzle breakdown during spray.
[e] Pressure increased during spray.

number of points located in a pore. The evaluation of the dendrite secondary arm spacing was made by searching for clearly visible dendrites in the cross-sections and directly measuring the secondary dendrite arm spacings averaged over several arms. The total fraction of aluminium and fraction of primary aluminium were also evaluated as functions of the layer thickness. This was madae using a randomly oriented 10 × 10 mesh and counting the points hitting the primary α-Al phase. The occurrence of other phases was measured as well, but not used at present.

4. Results and discussion

The results and discussion will be divided into six different parts. The process itself is treated in terms of material exchange, the formation of porosity and the level of porosity is described and the solidification characteristics in the process and the specifics of the solidification of the aluminium alloy itself are discussed. The fourth part is a theoretical treatment of the interaction between vacancies and the partition coefficient. The fifth part discusses the entrapment and condensation of vacancies. The sixth and last part is a general discussion of the vacancy model and a comparison with other existing models.

4.1. Process characteristics

The general appearance of a coating is shown in Fig. 2a and b. The figure shows two different coatings, sample SG8A1S9 and sample SG9A1S11. They both exhibit a fine structure in the region next to the substrate. This is because during the initial transient of the spray sequence the drops are formed by direct drop formation, a mechanism prevailing during low mass discharges and thus also a low thermal load on the substrate, yielding high cooling rates of the layer. The structure furthermore shows a slight decrease in secondary dendrite arm spacing with an increased distance from the substrate. This is because the metallostatic pressure decreases during spraying since the liquid height decreases, lowering the mass discharge and thus also the amount of heat that it is necessary to remove.

The basic issue concerning whether *in-situ* composites can be made is that the process itself is insensitive to the processing conditions. The presence of solid particles, when manufacturing *in-situ* composites, will increase the difficulties of creating a sound deposit. The sensitivity in the present study was taken as the material exchange defined as the mass percentage of sprayed material that solidified on the substrate. In Table 3 the material exchange is shown. Clearly the material exchange is well above 90% in all but three cases. The sample with the lowest material exchange was sample SG1A1S1. In this sample the pressure had to be continuously increased until a spray occurred. This was due to a freezing in the nozzle initially. As the pressure increased, some molten metal was released and finally as a sudden burst the melt was sprayed at the substrate. Thus it is likely that the flow initially was too low to make a continuous spray and the fraction of liquid was close to zero on substrate impact. As a massive spray was formed, most of the material was likely to stick to the substrate. This was confirmed using metallographic investigation by a wide and slightly random appearance of the secondary arm dendrite spacing as function of layer thickness, indicating large variations in the spray. The secondary dendrite arm spacing will be discussed in detail below. In sample SG6A1S7 the material exchange was somewhat higher than in sample SG1A1S7 but still low. This sample had a very low spraying temperature and driving gas pressure. They spray was here not formed by liquid film disintegration, but rather from direct drop formation. The droplets may thus have a higher solid fraction at the time of substrate impact. The formation of a substrate surface liquid film could not be sustained continuously. The material exchange was thus decreased by solid particles bouncing off the substrate on impact. Again this was confirmed by the fact that this sample had extremely fine secondary dendrite arm spacings, indicating a fine droplet size distribution. The third sample having less than the desired materials exchange was sample SG4A1S3. This sample was a low ratio, *l*/*d*, of the orifice length to orifice diameter of the nozzle, resulting in a lower nozzle flow drag coefficient and thus an increased mass discharge. The discharge is roughly linearly dependent on the drag coefficient, resulting in approximately a flow three to four times that of samples with similar characteristics [9]. A result here may be an increased fraction of very coarse droplets formed on disc impact. These droplets may have completely missed their target, lowering the yield. This was confirmed again by the secondary dendrite arm spacing, which showed a rapid increase initially, indicating an increased fraction of coarse droplets. As the liquid level inside the quartz tube increases, the metallostatic part of the driving pressure decrease and so also does the secondary dendrite arm spacing. All these three cases are to be regarded as anomalies in the process and are not representative of an optimized process. In general it may be concluded that in terms of material exchange the process is relatively insensitive to processing characteristics, if processed in the proper regime.

In the experiments both the spraying temperature and the applied pressure were varied. Excluding the anomalies above, the material exchange was well above 90%. It may thus be concluded that the material exchange is relatively insensitive to the thermal processing parameters. The most important factor at a given set-up is, as argued in the literature [9], the true width of the liquid pool at the point of impact between the jet and the disc. This is the key factor controlling the focusing of the spray and thus the real process material exchange in terms of mass hitting a non-circular target.

4.2. Porosity and substrate integrity

Powder metallurgy and spray forming suffer commonly from porosity. In spray forming, the porosity levels have decreased continuously as the technology advances. Today typical values for aluminium alloys in the as-sprayed condition are between 5 and 12%, under conditions similar to the present conditions [12]. Typical steady-state condition values are sightly lower than half that range. The present experimental set-up cannot be characterized as steady state since the spraying sequence was less than a second, the substrates were coated only with a layer, and no billet

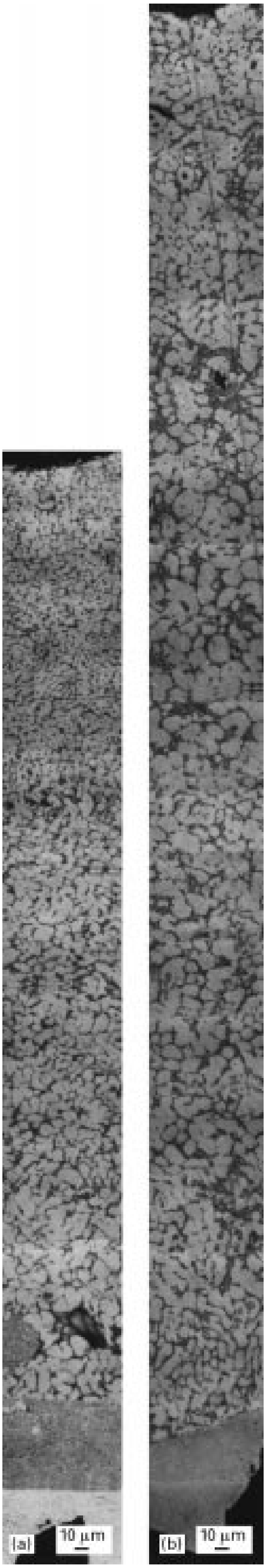

←

Figure 2 A cross-section of a sprayed layer illustrating the microstructural homogeneity of a sprayed layer and the low porosity attained. (a) sample SG89AlS9; (b) sample SG9AlS11. Note that the substrate is not included in the figures and only the deposit is shown.

TABLE III Experimental results

Experiment	Exit angle (deg)	Hoop spread (deg)	Material exchange (%)	Porosity (%)	Thermal load parameter (W kg^{-1})
SG1A1S1	106	57	42	2.25	31.5
SG1A1S2	118	91	95	3.00	157.1
SG4A1S3	142	132	83	2.25	34.9
SG5A1S4	107	108	95	9.25	43.7
SG3A1S5	191	70	95	4.50	102.8
SG6A1S7	132	96	62	4.75	1.3
SG7A1S8	109	129	95	2.00	10.0
SG8A1S9	104	110	91	3.75	7.2
SG9A1S11	91	141	98	2.00	47.0
SG1A1S13	120	96	96	1.50	7.5
SG10A1S12	125	114	93	2.75	7.8
SG6A1S14	132	119	98	4.75	10.3
SG6A6S15	107	137	94	2.00	21.3

was built up. The typical feature of a spray-formed body is the presence of a top and bottom porosity. In the present no bottom porosity was detected. In some samples a tendency towards a top porosity was found. In general the porosity may be described as distributed over the complete cross-section with a tendency to be more frequent at the top of the layer. The origin of the porosity is the balance between the thermal load on to the substrate and its capability to remove heat. Basically this is depending on the temperature of the melt to be sprayed and the mass flow. During spraying the droplets formed lose heat during flight. The amount of heat lost is proportional to the droplet size that in turn depends on both the mass flow and the rate of rotation. The mass flow from the nozzle onto the disk is depending on the length to width ratio and the pressure applied during spraying. Based on this it is possible to construct a thermal load parameter for a qualitative assessment of the thermal load during spraying. This may be written as

$$Q_{\text{load}} = \frac{2\pi C_{\text{p}}(T_{\text{spray}} - T_{\text{L}})\Delta P}{\omega(l/d)} \tag{1}$$

where T_{spray} (K) is the melt temperature during spraying, T_{L} (K) is the melt liquidus temperature, ΔP (atm) is the applied pressure, ω(rad s^{-1}) is the rate of rotation, l(m) is the length of the nozzle exit and d(m) is the diameter of the nozzle exit.

When Q_{load} is increased, the thermal load of the substrate increases and vice versa. Q_{load} is calculated for the experiments, (Table 3) and the correlation to the level of porosity is shown in Fig. 3. In the figure it is clear that all points but one follow a slightly U-shaped curve with a rapid increase in porosity towards low values of the thermal load parameter and slowly increasing towards high values. The point that is different originates from sample SG5A1S4. During spraying of this sample a possible temperature drop occurred and thus the thermal load parameter decreased and porosity increased. The real value of the thermal load parameter for this sample is thus lower than the calculated value.

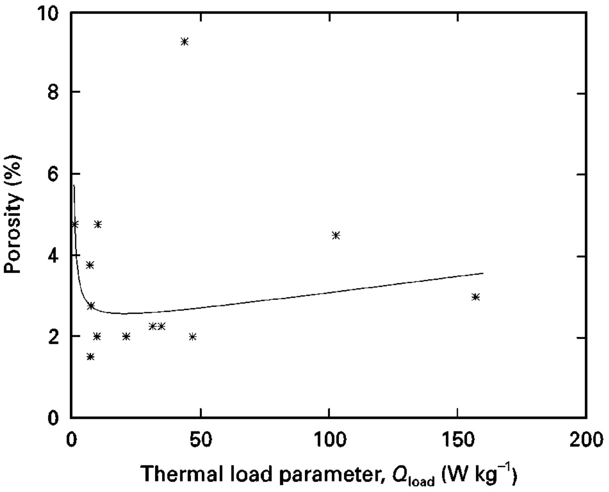

Figure 3 The porosity level as function of the thermal load parameter Q_{load} showing a slightly U-shaped dependence. The porosity was measured using a 20 × 20-point grid. The line shows the slightly U-shaped curve of the dependence and is given by (%Pores $= 22.2 + 0.0084/Q_{\text{load}} + 3.48Q_{\text{load}}$).

The reason for the U shape of the curve for the relation between the thermal load parameter and the porosity is due to two main factors. First the initial decrease in the porosity with an increased thermal load arises because the amount of solid in the droplets on impact decreases and a semisolid layer is built up. If the solid fraction is too high, the droplets will not spread and porosity will be entrapped. The main factor controlling this is the mass discharge. A small mass discharge creates small droplets and a small thermal load. The thermal load is small during the initial and the final transients, which explains why top and bottom porosity should be found. Bottom porosity was not found in the present study. A tendency towards top porosity could be detected. The influence of the metallostatic pressure has been neglected in the expression for the thermal load parameter. The metallostatic pressure is initially high. As all material is being sprayed, material is discharged and the metallostatic pressure decreases. The total driving pressure for the mass discharge and thus also a reduced thermal load of the substrate cause porosity to form. Most of the samples processed are on the left-hand side of the U-shaped region, which is why an increase in porosity is to be expected. This is the reason for the increased tendency towards top porosity. The increase in porosity towards high values for the thermal load parameter is less dramatic than that at low values. This indicates that the reason for the porosity is slightly different. The reason is thus not due to the state of the droplets on impact but rather the state of the substrate on impact. The deposited surface is not as smooth as the initial substrate and may be considered as a rough surface. A rough surface hinders the spreading of the droplets [12]. As the thermal load increases, the distance between each droplet in the spray decreases, owing to the increased mass flux. The interaction between the liquid droplets may thus also be important. The droplets may impinge on the substrate and collide, causing irregularities to form on the surface, and again these may hinder the spreading of the droplets on the substrate [12]. This causes porosity to form in the substrate at higher thermal load of the substrate.

4.3. Solidification

It must first be pointed out that each experiment produced a more or less homogeneous layer with variation originating from mass discharge and cooling behaviour of the droplets. In Fig. 2 a cross-section of the resulting deposit from sample SG811S9 is found, illustrating the appearance of a layer. At the bottom of the layer a region showing a fine structure is found arising from the initially low mass discharge due to an experimental disturbance initially. As the process starts, a fairly homogeneous structure is formed with a relatively low degree of porosity.

The dendrite secondary arm spacings were measured as a function of the distance from the bottom in all samples. All measurements made are found in Fig. 4. It is clear that there exist three main groups of arm spacing: one coarse, one moderate and one fine. Examples of these microstructures are shown in Fig. 5. The coarse structure and the moderate structure are distinguishable in thinner layers but, as the layer thickens, these groups coincide. This is most probably due to the interference from the liquid film formed on the layer surface; hence, most of the solidification takes place subsequently to substrate impact. The secondary arm spacing in a similar material (Al–6%Si) has been found to obey [13]

$$\lambda = 50 \times 10^{-6} \left(\frac{\mathrm{d}T}{\mathrm{d}t}\right)^{-0.33} \tag{2}$$

where λ (m) is the dendrite secondary arm spacing, T (K) is the temperature and t (s) is the time.

It must here be noted that the exact values for the cooling rates are not obtained but the order will be approximately the same. Dendrite arm coarsening is unlikely to occur because each experiment lasted of the order of 1 s. The use of the resulting dendrite secondary arm spacing will thus be a lower bound because if coarsening occurs, the spacing will be larger and thus the estimated cooling rate becomes lower. The resulting cooling rates calculated from the dendrite secondary arm spacing are shown in Fig. 6. The finer droplets impinging on the substrate tend to show a large spread in cooling rates. This difference is plausibly due to the larger degree of solidification during flight. Qualitatively the typical dendrite secondary arm spacing of 3 μm, 12 μm and 25 μm will thus correspond to cooling rates of 4630 K s^{-1}, 72 K s^{-1} and 8 K s^{-1}, respectively. This clearly indicates large differences in droplet size. The droplet cooling rate is approximately inversely proportional to the droplet diameter; thus the corresponding particle size ratios are 1 : 64 : 579. This is not the complete truth, since a large number of the droplets may have solidified partially before the impact on the substrate. The most interesting fact is that the estimate of 72 K s^{-1} of the average mainstream cooling rate indicates that rotary spray forming provides moderate cooling rates. Coupling the cooling rates to the microstructure it seem likely that most of the solidification will take place after impact owing to the lack of splat boundaries in the microstructure.

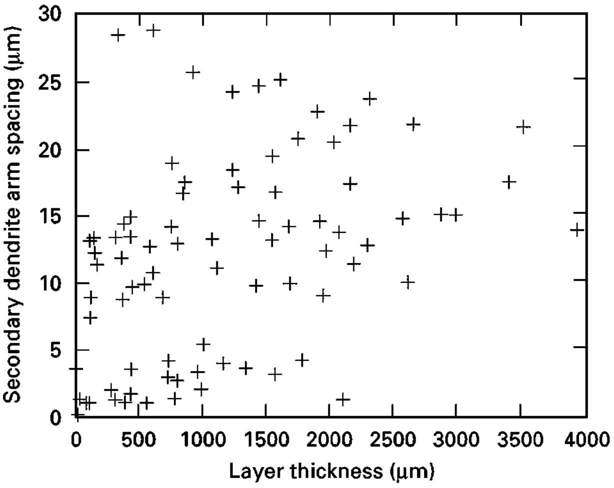

Figure 4 The dendrite secondary arm spacing found in the samples as a function of the layer thickness.

The cooling rates found were moderate for spray processing but still fairly high compared with the cooling rates found in a traditional casting processes. The cooling rates indicate that solidification takes place relatively rapidly. The rapid processing yields a condition where the solidification takes place more or less without solid-state diffusion of the dissolved species. From this point of view it seems reasonable that the alloy should obey the Scheil equation in terms of fractions and partition coefficients. It should here be noted that the partition coefficients obtained in this way is to be regarded as an effective partition coefficient. The Scheil equation may be written as

$$X^{\mathrm{L}} = X^{0}(1 - f^{\mathrm{p}})^{(k^{S-L} - 1)} \tag{3}$$

where X^{L} is the concentration in the liquid (here the eutectic composition), X^{0} is the nominal concentration, f^{p} is the fraction of solid (at the eutectic point

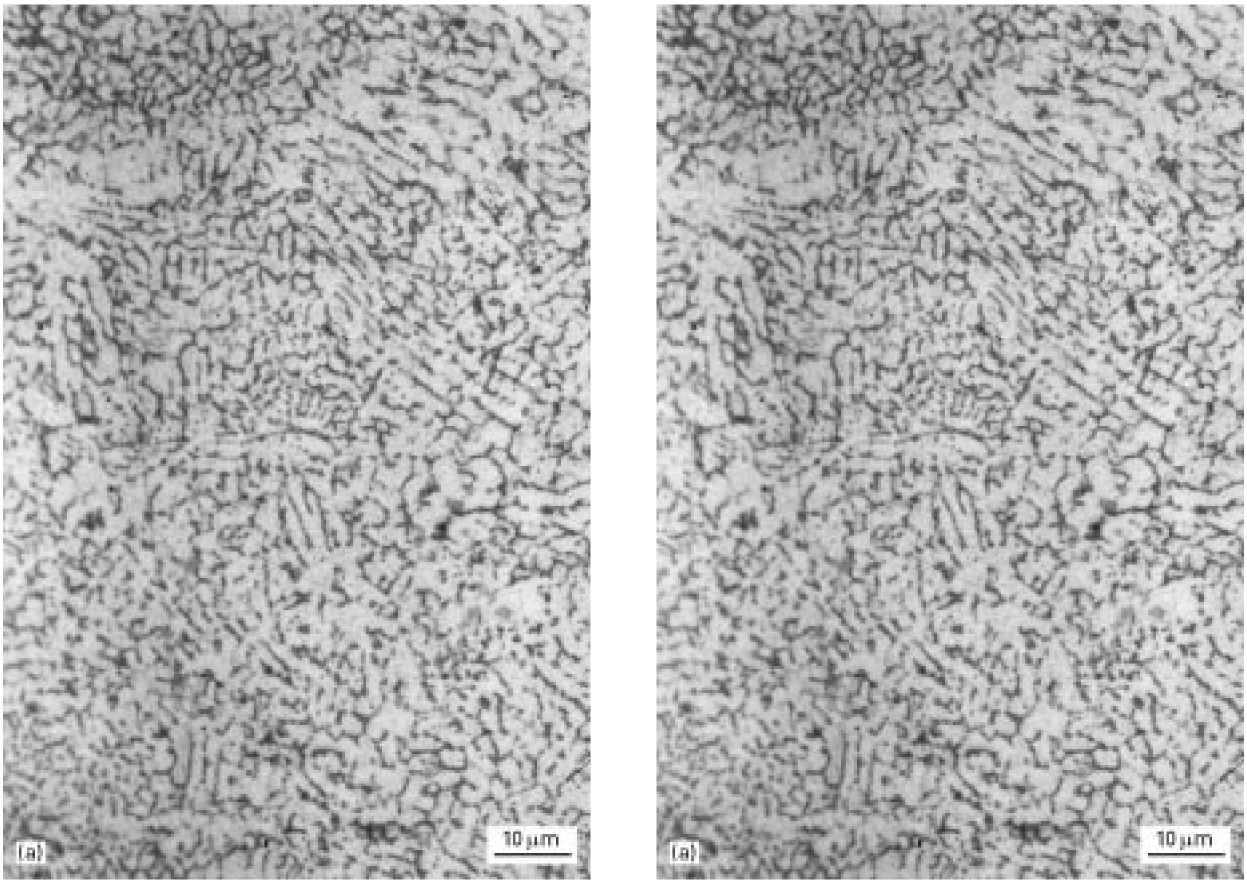

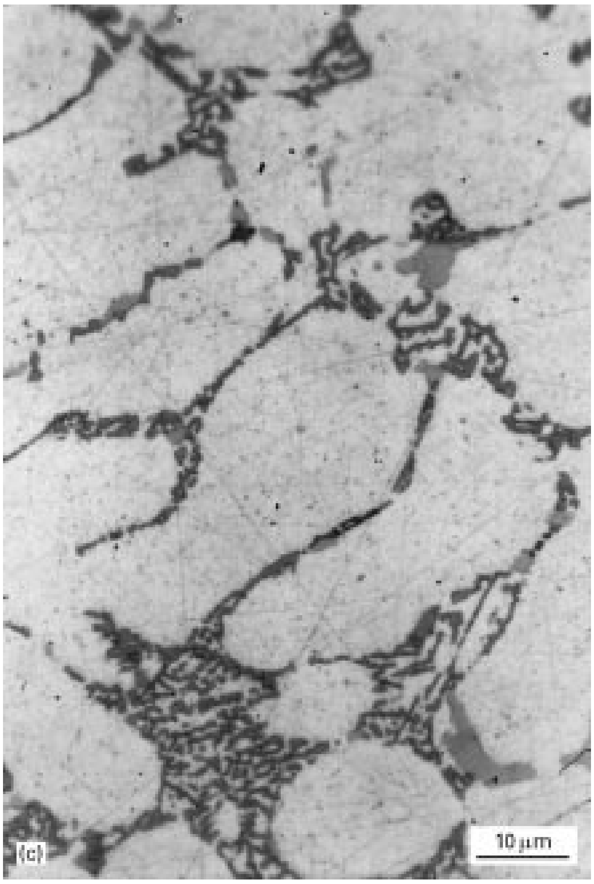

Figure 5 (a) Micrograph showing the fine microstructure, sample SG3AlS5; (b) micrograph showing the intermediate-scale microstructure, sample SG1AlS13; (c) micrograph showing the coarse structure, sample SG7AlS8.

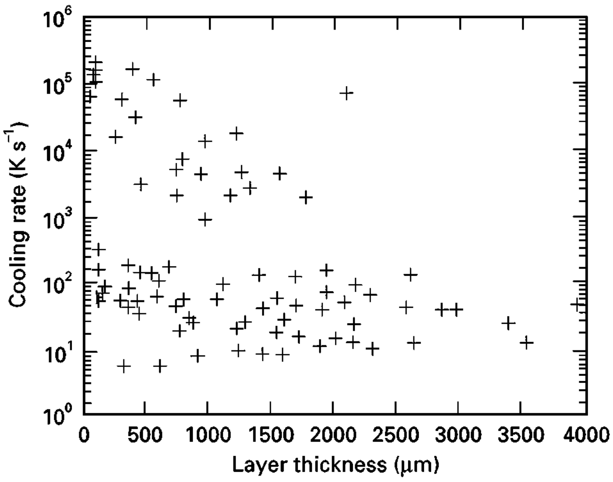

Figure 6 Calculated cooling rates from the secondary dendrite arm spacing using Equation 1 and the experimentally obtained dendrite arm spacings.

this is the fraction primary precipitates) and k^{S-L} is the partition coefficient.

The primary fraction of precipitated aluminium was evaluated as a function of the layer thickness (Fig. 7a). The eutectic composition naturally depends on the process conditions. The main stream conditions with a typical cooling rate of $72\,\mathrm{K\,s^{-1}}$ is, however, not extreme and the effect on the eutectic composition will be limited. Under these conditions the assumption that the liquid eutectic composition does not alter seems reasonable. The partition coefficient can thus be calculated from the fraction of primary phase and the eutectic composition. Surprisingly the value is

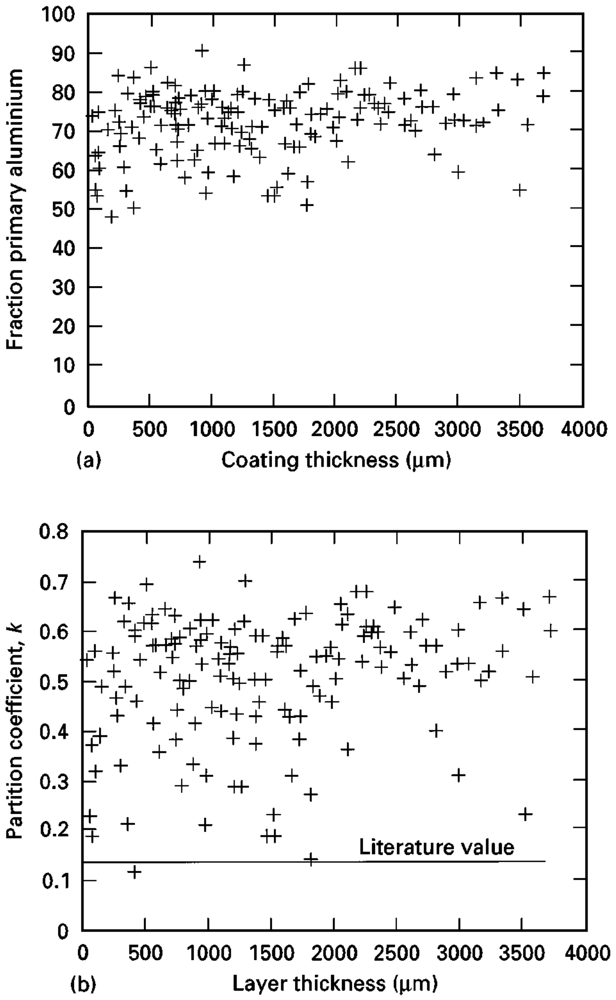

Figure 7 (a) Fraction of primary aluminium measured in the experiments using the 10×10 point grid. (b) Partition coefficient as function of layer thickness calculated using the Scheil Equation 2 from the fraction of primary α-Al phase using the eutectic concentration and initial concentration of the alloy.

substantially different from the values found in the literature. There also seem to exist some kind of saturation value between 0.6 and 0.7 (Fig. 6b). In the ternary Al–Si–Mg system the partition coefficient between the liquid and the solid may have values between 0.052 and 0.131 dependent upon the solidification path [14]. The value of the partition coefficient depends on which of the two different existing eutectic routes are taken. The lowest value is for the quasibinary eutectic with Al + Mg_2Si. The partition coefficient, at the point of the ternary eutectic, is 0.088. In the binary Al–Si system the partition coefficient is 0.131. Independent of this, the maximum equilibrium value is 0.131. The microstructure of the solidified layers show that the solidification is primarily binary and consists of α-Al and Si. The ratio of the saturation value for the effective partition coefficient as indicated by Fig. 7b, to the binary partition coefficient, i.e. $k/k^0 = 0.65/0.131 = 4.96$, shows that close to a fivefold change in the partition coefficient has occurred. This is a maximum value for the prevailing cooling rates. It has recently been discussed that the partition coefficient and the phase diagrams may be substantially altered by the presence of vacancies [15–17]. These vacancies are formed in large numbers during solidification. During solidification they will either diffuse back toward the liquid–solid interface or condense, forming dislocations, grain boundaries and cracks. This has also been experimentally verified by Imura *et al.* [18]. Imura *et al.* [18] made *in-situ* observations of solidification in metals, using an X-ray technique identifying dendrites and dislocations. They found that there existed a dislocation-free zone behind the growth front and thus also an incubation time for these defects to form. This is decisive evidence of the fact that vacancies are caught at the growth front and condense as dislocations as one possible sink. The presence of these trapped vacancies also causes the heat of fusion to change. The vacancies will increase the free energy of the solid and thus also the heat release during solidification. Since the amount of vacancies trapped is a function of the cooling rate, properties such as the heat release during solidification are dependent on the cooling rate. As the material cools, the vacancies condense into structural defects, lowering the free energy of the solid, and thus most of the residual heat of fusion is regained.

The presence of excess vacancies will change the phase diagram. In general, the effect will decrease the melting point of the pure element. In an alloy the case is similar with a change in the slopes of the liquids and solids lines, and thus a change in partition coefficient. The fraction of primary aluminium may thus be increased, yielding a high partition coefficient when using the Scheil equation to evaluate the effective partition coefficient.

4.4. Theoretical treatment of the partition coefficient

The aim of this treatment is to calculate the influence of vacancies on the partition coefficient, as well as to estimate the interaction parameter between Si and vacancies using a Wagnerian formalism.

The partition coefficient for Si in Al, involving vacancies is defined as [19]

$$\begin{aligned} k &= \frac{X_{\text{Si}}^{\text{solid}}}{X_{\text{Si}}^{\text{liquid}}} \\ &= \frac{\gamma_{\text{Si}}^{\text{liquid}}}{\gamma_{\text{Si}}^{\text{solid}}} \exp\left(-\frac{{}^0G_{\text{solid}} - {}^0G_{\text{liquid}} + (X_{\text{vac}} - X_{\text{vac}}^{\text{eq}})G_{\text{vac}}}{RT}\right) \end{aligned} \tag{4}$$

where G (J mol^{-1}) is the Gibbs free energy, γ is the activity coefficient and R (J mol^{-1} K^{-1}) is the general gas constant.

The activity coefficient in the solid can be expressed using a Wagnerian type of expression

$$\gamma_{\text{Si}}^{\text{solid}} = \gamma_{\text{Si}}^{0} \exp(X_{\text{Si}}\,\varepsilon_{\text{Si}}^{\text{Si}} + (X_{\text{vac}} - X_{\text{vac}}^{\text{eq}})\,\varepsilon_{\text{Si}}^{\text{vac}}) \tag{5}$$

where ε is the Wagnerian interaction coefficient.

Inserting equation (5) into equation (4) and identifying the partition coefficient for an alloy with an equilibrium concentration of vacancies yields [19]

$$k = k^0 \exp\left[-(X_{\text{vac}} - X_{\text{vac}}^{\text{eq}})\left(\frac{G_{\text{vac}}}{RT} + \varepsilon_{\text{Si}}^{\text{vac}}\right)\right] \tag{6}$$

where k^0 is the equilibrium partition coefficient.

Now $G_{vac} = \Delta H_{vac} - T\,\Delta S_{vac}$ for which data are accessible from [17]. The remaining difficulty is to estimate the interaction coefficient ε. In the paper by Gorecki [20], two models are compared, originating from the works of Lomer [21] and Schapink [22]. These state that the ratio of the concentration of vacancies in an alloy to that in a pure metallic substance is given by the following equations: according to Lomer [21],

$$\frac{X_{vac}^{Al-Si}}{X_{vac}^{Al}} = 1 - ZX_{Si} + ZX_{Si}\exp\left(\frac{E}{kT}\right) \qquad (7)$$

and, according to Schapink [22],

$$\frac{X_{vac}^{Al-Si}}{X_{vac}^{Al}} = 1 + X_{Si}\left[\exp\left(\frac{E}{kT}\right) - 1\right]^{z} \qquad (8)$$

where Z is the coordination number, E (J) is the vacancy–solute binary interaction energy and k (J K^{-1}) is Boltzmann's constant.

On the other hand, treating vacancies as any kind of dissolvable species, the ratio may be expressed by using a Wagnerian formalism and neglecting Si–Si interaction. Equilibrating one piece of pure Al and one piece of Al–Si the activity of vacancies will be equal but the concentration of vacancies will be different. Under these assumptions the same ratio as in Equations 7 and 8 may be used to yield the expression for the interaction coefficient between Si and vacancies using the Wagnerian formalism:

$$\frac{X_{vac}^{Al-Si}(X_{Si} \neq 0)}{X_{vac}^{Al}(X_{Si} = 0)} = \frac{a_{vac}^{Al-Si}}{a_{vac}^{Al}}\,\frac{\gamma(X_{Si} = 0)}{\gamma(X_{Si} \neq 0)} = \frac{\gamma(X_{Si} = 0)}{\gamma(X_{Si} \neq 0)} = \exp(-\varepsilon_{vac}^{Si} X_{Si}) \qquad (9)$$

where a is the chemical activity.

Using Lomer's [21] model the interaction coefficient can be assessed by setting Equation 7 equal to Equation 9 and rearranging, yielding

$$\varepsilon_{vac}^{Si} = \frac{1}{X_{Si}}\,\mathrm{In}\left[1 - ZX_{Si} + ZX_{Si}\exp\left(\frac{E}{kT}\right)\right] \qquad (10)$$

Following the line of Gorecki [20], who stated that the true interaction energy is found by taking the limit where $X_{Si} \to 0$, the same must be valid for the interaction coefficient

$$\lim_{X_{Si}\to 0}(\varepsilon_{vac}^{Si}) = \varepsilon_{vac}^{Si} = Z\left[1 - \exp\left(\frac{E}{kT}\right)\right] \qquad (11)$$

In the work by Gorecki [20] the binary interaction energy between vacancies and silicon in aluminium was given as 0.159 eV, using this and the fact that coordination number in aluminium is 12, the interaction coefficient can now be calculated. The result of the calculation is shown in Fig. 8. The partition coefficient has been experimentally determined in the present work. Using the fact that $\varepsilon_{vac}^{Si} = \varepsilon_{Si}^{vac}$ it is now possible to calculate the increase in vacancy concentration necessary to change the partition coefficient using Equations 11 and 6. The result is shown in Fig. 9, where the relative change is calculated for three different temperatures. The necessary fraction of vacancies to obtain the same ratio k/k^0 as in the experiments is in the range 0.019–0.025 depending on the temperature for solidification. The amount of vacancies necessary is thus roughly 0.02.

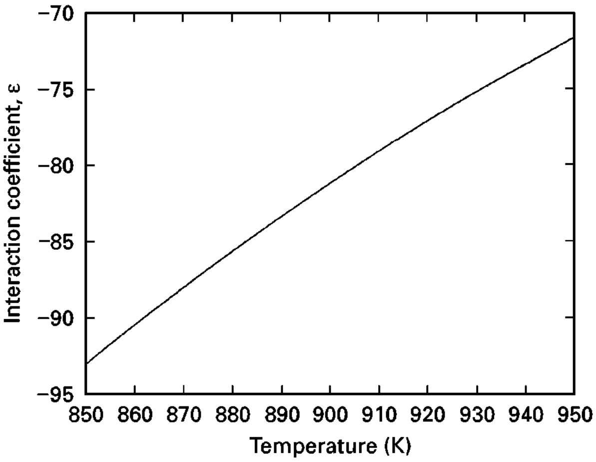

Figure 8 Calculated Wagnerian interaction coefficient calculated from Equation 1.

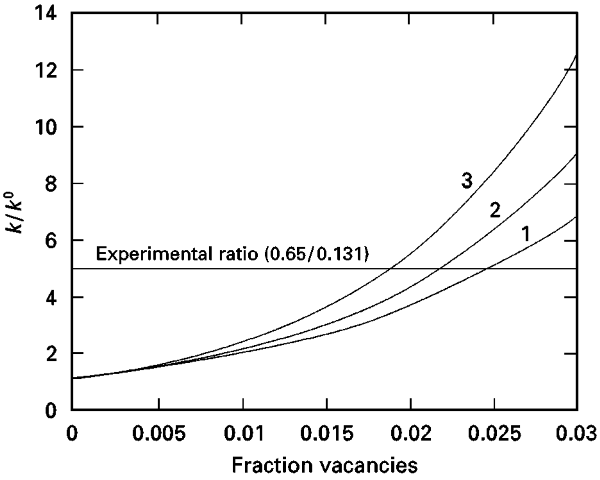

Figure 9 Partition coefficient ratio, k/k^0, as a function of the fraction vacancies at $T = 900$ K (curve 1), $T = 850$ K (curve 2) and $T = 800$ K (curve 3). The horizontal lines are the experimentally obtained values and the curves are the values obtained from Equation 5 using the value of the interaction coefficient obtained by Equation 10.

4.5. Entrapment and condensation of vacancies

As solidification takes place, shrinkage occurs. This shrinkage must occur over the solid–liquid interface. A certain number of vacancies is being caught at the interface and has to diffuse to some sink, i.e., dislocation grain boundaries and the solid–liquid interface. The maximum amount of vacancies being caught at the solidification front is the same as that of the volume change during solidification, i.e. for the present kind of alloy system [23]:

$$X_{vac}^{max} = \frac{\rho_{solid} - \rho_{liquid}}{\rho_{solid}} \approx 0.07 \qquad (12)$$

A large portion of these vacancies will be present at the solid–liquid interface and thus alter the surface

TABLE IV Diffusivity at 900 K

Diffusing element	Diffusivity ($m^2\,s^{-1}$)
Al [23]	9.3×10^{-13}
Si [23]	2.8×10^{-12}
Si–vacuum pair [24]	1.8×10^{-13}–3.6×10^{-11}

tension of the interface, yielding changes in the interfacial concentration. Neglecting the surface tension effects the first issue is to determine the fraction vacancies being caught at the growth front. The solidification shrinkage shall occur over the interface. The fraction of vacancies being caught at the growth front has been treated thoroughly by Van Siclen and Wolfer [24] as well as by Bolling and Fainstein [25]. Van Siclen and Wolfer [24] calculated the fraction vacancies in Ni droplets and found that the vacancy fraction could be as high as 0.056 during their study. Bolling and Fainstein [25] used a simplistic approach giving the fraction of vacancies being caught as

$$X_{\text{vac}} = X_{\text{vac}}^{\text{eq}} + \frac{X_{\text{vac}}^{\text{liquid}}}{1 + D^{\text{I}}/v\delta} \tag{13}$$

where $v(\text{m}\,\text{s}^{-1})$ is the growth velocity, $\delta(\text{m})$ is the interface width (approximately four atomic distances for aluminium [25]) and $D^{\text{I}}(\text{m}^2\,\text{s}^{-1})$ is the interface diffusivity.

The diffusivity for self-diffusion and tracer impurity diffusion in aluminium at 900 K are found in Table 4 [26]. The Si–vacancy pair diffusivity was calculated using the results of Ozawa and Kimura [27] and the binary interaction energy found by Gorecki [20]. The diffusivity is highly dependent on the vacancy concentration. The main result is, however, that the interfacial diffusivity may be as low as of the order $10^{-13}\,\text{m}^2\,\text{s}^{-1}$ and as high as $10^{-11}\,\text{m}^2\,\text{s}^{-1}$. These values may be regarded as upper and lower bounds for the diffusivity.

To correlate the cooling rates estimated and the growth velocity the effect of vacancies must be taken into account. The vacancies will increase the free energy of the solid and thus decrease the energy difference between the solid and the liquid. The relation between the atomic bonding energy and the enthalpy may be expressed as [28]

$$\Delta H_{\text{i}} \approx (Z)^{1/2}\,|U_{\text{bonding}}| \tag{14}$$

where $\Delta H_{\text{i}}(\text{J atom}^{-1})$ is the enthalpy and U_{bonding} (J atom^{-1}) is the bond energy.

The effect of the vacancies is to change the coordination number of the atoms; therefore, the relation between the solid enthalpy and the enthalpy of the vacancy per atom may be expressed as for a monovacancy:

$$\frac{\Delta H_{\text{vac}}}{\Delta H} \approx \left(\frac{Z-1}{Z}\right)^{1/2} \tag{15}$$

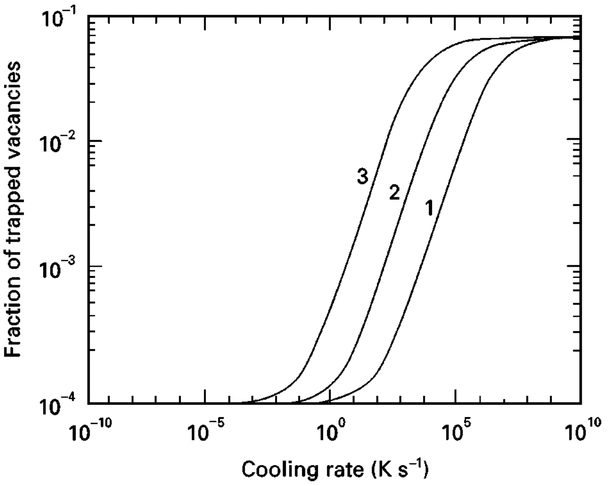

Figure 10 The fraction of vacancies being caught at the growth front as a function of cooling rate. The calculation is made for three different diffusivities $D = 10^{-11}\,\text{m}^2\,\text{s}^{-1}$ (curve 1), $10^{-12}\,\text{m}^2\,\text{s}^{-1}$ (curve 2) and $10^{-13}\,\text{m}^2\,\text{s}^{-1}$ (curve 3).

The local time for solidification may thus be expressed as

$$t_{\text{solidification}} = \frac{(-\Delta H)(1 - X_{\text{vac}}[(Z-1)/Z]^{1/2})/C_{\text{p}} + \Delta T}{\left(\dfrac{\mathrm{d}T}{\mathrm{d}t}\right)} \tag{16}$$

where $\Delta H(\text{J kg}^{-1})$ is the latent heat of fusion, $C_{\text{p}}(\text{J kg}^{-1}\,\text{K}^{-1})$ is the specific heat, $\Delta T(\text{K})$ is the solidification interval and $t_{\text{solidification}}(\text{s})$ is the local solidification time.

Locally the relation between the solidification time and the growth velocity, under the assumption of constant growth velocity, is given by

$$v \approx \frac{\lambda}{2t_{\text{solidification}}} \tag{17}$$

Under these assumptions the fraction vacancies being caught can be calculated using Equations 2, 13, 16 and 17. The result from such a calculation is shown in Fig. 10. The mainstream of droplets had cooling rates of the order of $10^2\,\text{K}\,\text{s}^{-1}$. For the lowest diffusivity $(10^{-13}\,\text{m}^2\,\text{s}^{-1})$ it is clear that this may cause a fraction of vacancies of the order of 0.008. The more rapidly cooled part of the samples (greater than $4\,10^4\,\text{K}\,\text{s}^{-1}$) will yield between 0.03 and 0.04, with the same order of entrapped vacancies at $10^{-12}\,\text{m}^2\,\text{s}^{-1}$. From these facts and the uncertainties in the calculations, it may be concluded that it is possible to obtain locally these very high fractions of vacancies and thus also a great influence on the partition coefficient. These results are also in accordance with the findings for nickel by Van Siclen and Wolfer [24]. They found a large fraction of vacancies in the interface of solidifying nickel. The increase in the fraction was local, which may be attributed to the large mobility of atom–vacancy pairs. The exact nature of the entrapment will also depend on exactly how the shrinkage is accommodated across the solid–liquid interface.

A lattice filled with a large fraction of vacancies would produce a situation in which the diffusion can

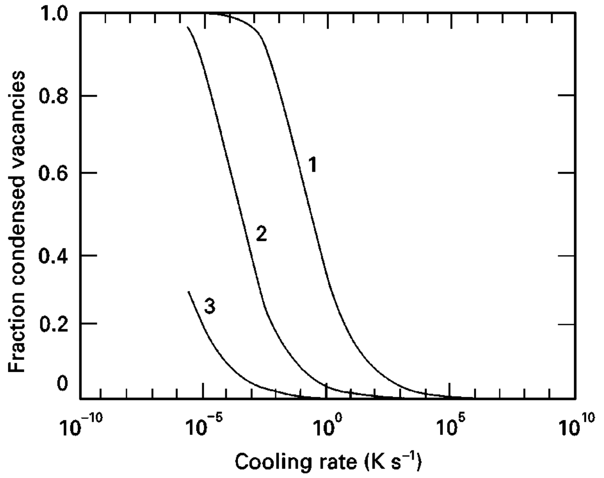

Figure 11 Fraction of condensed vacancies calculated with Equations 1, 12 and 13. The calculation is made for three different diffusivities $D = 10^{-11}\,\mathrm{m^2\,s^{-1}}$ (curve 1), $10^{-12}\,\mathrm{m^2\,s^{-1}}$ (curve 2) and $10^{-13}\,\mathrm{m^2\,s^{-1}}$ (curve 3).

be extremely rapid. The condensed fraction of the initial concentration of vacancies, as a function of time, in a system showing periodic concentration differences is approximately given as

$$f = 1 - \exp\left(-\frac{\pi^2 D t}{4\lambda^2}\right) \tag{18}$$

Under the assumption that the effective distance is the same as the dendrite secondary arm spacing and that the time for homogenization or condensation time is the same as the local solidification time, the fraction of condensed vacancies can be calculated. The result of the calculation is shown in Fig. 11. From the figure it is clear that a fraction of less than 0.08 and 0.03 may condense during solidification for the main stream droplets and for the fine droplets, respectively.

It may thus be concluded from the tendencies found at present and in the literature [15–18, 20–22, 24, 25] that the partition coefficient is greatly affected by the presence of entrapped vacancies. These vacancies are entrapped and under the present conditions they will not condense or annihilate during solidification.

4.6. Comparison with other models concerning the kinetic aspects of solidification

Many attempts have been made during the last few years to describe the change in the partition coefficient due to kinetic effects. A model that has won fairly general acceptance is the continuous growth model developed by Aziz [29] and Aziz and Kaplan [30]. The continuous growth model is a phenomenological description of the kinetic aspects of solidification. The general feature of a phenomenological description is that it quite well may describe the effects but yields little information on the real physical events. This has also been pointed out by Jackson *et al.* [31] concerning the continuous growth model. The key parameter of the continuous growth model is the so-called diffusive speed, i.e., the ratio of the interfacial diffusivity to the interface width. It is clear that the effective partition coefficient is inversely proportional to the diffusive speed, as demonstrated by Aziz [29]. Aziz [29] furthermore clearly shows that there is no similar dependence between the solid, liquid and geometric mean of the solid and liquid diffusivity with the diffusive speed. This is decisive evidence that purely kinetic reasoning is insufficient. The vacancy entrapment will, from a kinetic point of view, explain the change in diffusivity in the interface region because the diffusivity is proportional to the vacancy concentration [27]. Given that the equilibrium concentration of vacancies at the liquidus temperature is of the order of 10^{-4} and that the kinetic concentration is two orders of magnitude greater, the interfacial diffusivity will be expected to attain a similar increase. Since the vacancy concentration depends on the processing conditions, the interfacial diffusivity will also depend on the processing condition. The vacancy model will furthermore take thermodynamic effects into account through the interaction coefficient between solute and vacancy. During the manufacture of ordered compounds, disorder trapping occurs and was treated by Boettinger and Aziz [32]. Disorder trapping arises because the solidified compound will inherit the disorder of the melt. This type of disorder is easily measurable because the atoms normally are located in two different sublattices. In a disordered solid solution the situation is slightly different. Vacancy entrapment in a disordered solution is similar to freezing of the liquid disorder into the solid. It is, however, unlikely that the liquid disorder would be inherited only during the processing of ordered compounds and not during the processing of disordered compounds. The inheritance of the liquid disorder in a disordered compound is a difficult feature to measure. The freezing of the liquid disorder into the solid will, however, increase the free energy of the solid, lowering the heat evolved during solidification, as clearly demonstrated by Berg *et al.* [17], which indirectly proves the existence of disorder inheritance.

5. Concluding Remarks

The rotary spray former at present used may be utilized for both powder manufacturing and coating. In the case of the manufacture of coatings, the sensitivity of the ability for a layer build-up is relatively insensitive to the thermal conditions, which is an advantage in microstructural control. The thermal insensitivity allows the process to work in a wide temperature range of superheat. The porosity levels obtained must be regarded as low for the spray forming of aluminium.

The cooling rates found in rotary spraying are fairly high but not extreme. In the present process, indirect observation of the cooling rates was made. The technique used was first to measure the secondary dendrite arm spacing and then to convert this to cooling rates. The three typical orders of dendrite secondary arm spacing were found to be 3 μm, 12 μm and 25 μm. The corresponding cooling rates were found to be $4630\,\mathrm{K\,s^{-1}}$, $72\,\mathrm{K\,s^{-1}}$ and $8\,\mathrm{K\,s^{-1}}$, respectively.

A well-established fact in the present study is the large influence of vacancies on the microstructure at moderate to high cooling rates. The reason behind this is the vacancies being caught at the growth front. Some of these vacancies are being condensed at the solid liquid interface or as dislocations, stacking faults and so on. The key point is the fraction vacancies at the growth front. In the present study, surface tension has been neglected and this is why more work is needed to establish dynamic surface tensions during solidification. This has to do with the nature of the accomodation of shrinkage over the interface.

Acknowledgements

The present work has been sponsored by the Carl Trygger Foundation. The author is deeply indebted to Professor Hasse Fredriksson, at Kungliga Tekniska Högskolan, for his great support, guidance and brilliant ideas. The author is also indebted to Mr Johan Dahlström, at Kungliga Tekniska Högskolan, for stimulating discussions and support with literature.

References

1. A. R. E. SINGER, *J. Inst. Metals* **100** (1972) 185.
2. *Idem*., *Mater. Sci. Engng* **A135** (1991) 185.
3. E. J. LAVERNIA, E. M. GUITERREZ-MIRAVETE, J. SZEKELY and N. J. GRANT, *Int. J. Rapid Solidification* **4** (1988) 89.
4. E. M. GUITERREZ-MIRAVETE, E. J. LAVERNIA, G. M. TRAPAGA and J. SZEKELY, *ibid.* **4** (1988) 125.
5. E. M. GUITERREZ-MIRAVETE, E. J. LAVERNIA, G. M. TRAPAGA, J. SZEKELY and N. J. GRANT, *Metall. Trans. A* **20** (1989) 71.
6. X. ZENG, H. LIU, M. G. CHU and E. J. LAVERNIA, *ibid.* **23** (1992) 3394.
7. X. ZENG, H. LIU and E. J. LAVERNIA, in "Metal matrix composites", Vol. 1, Proceedings of Ninth International Conference on Composite Materials, edited by A. Miravete, University of Zaragosa, Zaragosa, Spain (1993).
8. A. E. W. JARFORS, in "Spray processing", Proceedings of the Sefström Symposium, Royal Institute of Technology, Department of Metallurgy, 1994, pp. 305–324.
9. A. E. W. JARFORS, *Journal of Materials Processing* **71** (1997) pp. 440–455.
10. German Patent 116, 698–1899 (1899).
11. German Patent 24, 460–1882 (1882).
12. E. J. LAVERNIA and Y. WU, "Spray atomization and deposition" (Wiley, Chichester, West Sussex, 1996).
13. S. SU, X. LIANG, A. MORAN and E. J. LAVERNIA, *Int. J. Rapid Solidification* **8** (1994) 161.
14. "Metals handbook", Volume 8, "Metallography, structures and phase diagrams" (8th Edn, 1973) pp. 396–397.
15. N. EL-MAHALLAWY, M. TAHA and H. FREDRIKSSON, *Mater. Sci. Engng* **A179–A180** (1994) 587.
16. M. HADDAD-SABZEVAR and H. FREDRIKSSON, *Metall. Trans.* (1998) in press.
17. S. BERG, J. DAHLSTRÖM and H. FREDRIKSSON, *Iron Steel Inst. Jpn. Int.* **35** (1995) 876.
18. T. IMURA, H. SAKA, T. KOBAYASHI, N. KAWABE, A. SAKAI and H. SUGA, *Mem. Facul. Engng, Nagoya Univ.* **39** (1987) 195.
19. H. FREDRIKSSON and U. ÅKERLIND, Unpublished work (1996).
20. T. GORECKI, *Ber. Bunsenges. Phys. Chem.* **87** (1983) 801.
21. W. M. LOMER, "Vacancies and other point defects in metals and alloys" (Institute of Metals, London, 1958) p. 79.
22. F. W. SCHAPINK, *Phil. Mag.* **12** (1965) 1055.
23. D. ALTENPOHL, "Aluminium viewed from within" (Aluminium-Verlag, Düsseldorf, 1982) p. 74.
24. C. DeW. VAN SICLEN and W. G. WOLFER, *Acta Metall. Mater.* **49** (1992).
25. G. F. BOLLING and D. FAINSTEIN, *Phil. Mag.* **25** (1972) 45.
26. E. A. BRANDES and G. B. BROOK (eds), "Smithell's metals reference book", Butterworth–Heinemann, Oxford, 7th Edn, (1992).
27. E. OZAWA and H. KIMURA, *Acta Metall.* **18** (1970) 995.
28. V. HEINE and HAFNER, in "Proceedings of the Conference on Many-Atom Interactions in Solids", edited by R. M. Nieminen, M. J. Puska and M. J. Manninen, Pajulahti, 5–9 June (1989) pp. 12–31.
29. M. J. AZIZ, *Metall. Trans. A* **27** (1996) 671.
30. M. J. AZIZ and T. KAPLAN, *Acta Metall.* **36** (1988) 2335.
31. K. A. JACKSON, G. H. GILMER and D. E. TEMKIN, *Phys. Rev. Lett.* **75** (1995) 2530.
32. W. J. BOETTINGER and M. J. AZIZ, *Acta Metall.* **37** (1989) 3379.

Received 28 May 1997
and accepted 11 May 1998